

## Full Length Article

# Effect of oxygen concentration and N<sub>2</sub>-substitution on soot formation of a coflow oxy-fuel CH<sub>4</sub> laminar diffusion flames

Muhammad Bukar <sup>a</sup> , Suman Basnet <sup>a</sup> , Peng Liu <sup>b</sup>, Gaetano Magnotti <sup>a,\*</sup> <sup>a</sup> Physical Science and Engineering Division, Clean Combustion Research Centre, King Abdullah University of Science and Technology, Thuwal 23955, Saudi Arabia<sup>b</sup> State Key Laboratory of Clean Energy Utilization, Zhejiang University, Hangzhou 310027, China

## A B S T R A C T

Oxy-fuel combustion is a promising strategy for reducing greenhouse gas emissions and improving carbon capture efficiency by burning fuels in an atmosphere of pure oxygen and recycled gas (CO<sub>2</sub>) instead of air. Understanding soot formation in oxy-combustion systems is crucial for minimizing pollutant emissions and enhancing overall efficiency. This study experimentally examines the effect of oxygen concentration and nitrogen substitution on the sooting behavior of laminar coflow oxy-CH<sub>4</sub> diffusion flames with O<sub>2</sub>/CO<sub>2</sub> as the oxidizer. The sooting propensity of flames burning in O<sub>2</sub>/CO<sub>2</sub> and O<sub>2</sub>/N<sub>2</sub> atmospheres were compared at constant adiabatic flame temperature and oxygen concentrations. PAH Planar Laser-Induced Fluorescence (LIF) was used to investigate the effect of the parameters above on soot precursors, and Laser-Induced Incandescence (LII) calibrated using the Light Extinction Method (LEM) was employed for planar distribution of soot volume fraction. DSLR imaging and OH\* chemiluminescence provide the flame height and topology. The measured flame heights were correlated to several theoretical models in the literature and were found to decrease monotonically. Our results showed that increased oxygen concentration enhanced PAH concentration and sooting tendency only up to a certain point above which soot is diminished. This trend persists for various soot parameters such as the centerline, peak, maximum soot yield, radially integrated, and volumetrically integrated soot volume fraction. The results further showed a consistently higher soot yield for O<sub>2</sub>/N<sub>2</sub> flames over O<sub>2</sub>/CO<sub>2</sub> flames, and that was explained by the chemical and thermal effect of CO<sub>2</sub> in suppressing soot, in addition to the shorter residence time in CO<sub>2</sub> flames. This study offers valuable insights into the relationship between oxidizer composition and sooting tendency in oxy-fuel combustion while providing data sets for validating numerical models.

## 1. Introduction

Oxy-fuel combustion [1] is a promising technology for Carbon Capture and Storage (CCS) [2] and climate change mitigation. Oxy-fuel combustion is a process in which fuel is combusted in an environment with pure oxygen (O<sub>2</sub>) and recycled flue gas, such as carbon dioxide (CO<sub>2</sub>), instead of air. The recirculation of CO<sub>2</sub> is done to control the flame's overall temperature. Oxy-combustion provides higher efficiency and the elimination of NO<sub>x</sub> by virtue of N<sub>2</sub> absence in the combustion environment. Thus the products of combustion will mainly consist of CO<sub>2</sub> and water vapor (H<sub>2</sub>O), which can be easily separated through water condensation.

Soot poses a significant adverse effect on human health [3,4] and it contributes to global warming [5]. Hence, understanding the formation and oxidation of soot in oxy-combustion, is essential to mitigate its effect on health and the environment, when adopting this promising CCSU approach.

To optimize efficiency, various oxy-combustion technologies are operated at high [6] or extreme pressures [7] in turbulent conditions. However, due to reduced residence times, high intermittency, and

additional challenges associated with measurements in turbulent conditions, most soot studies in the literature are carried out at laminar conditions. By utilizing the laminar flamelet approximation [8], turbulent flames can be assumed to be ensembles of strained laminar flamelets. This approximation makes studying laminar flames with easily controlled boundary conditions useful for practical applications.

A critical parameter that can be varied in the study of soot in oxy-fuel combustion is the oxidizer O<sub>2</sub>/CO<sub>2</sub> ratio. An increase in O<sub>2</sub>/CO<sub>2</sub> ratio promotes high flame temperatures and hence can accelerate soot formation on the fuel-rich side and oxidation on the lean side of a diffusion flame [9,10]. The presence of CO<sub>2</sub> itself, through its intrinsic radiative and chemical properties, can affect the various stages of soot formation.

Several studies have investigated the effect of O<sub>2</sub> concentration (OC) on soot formation in the coflow flames. Lee et al. [11] studied the impact of OC in the oxidizer stream of methane in an oxygen-enriched air environment. In addition to the air baseline flame, they looked at two other flames with O<sub>2</sub> mole fractions of 50 % and 100 % using the Light Extinction technique. Their results showed that total soot yield decreases with increased O<sub>2</sub> concentration. Sun et al. [12] varied OC from 21 % to 36.9 % in ethylene laminar coflow flame using a Santoro-style

\* Corresponding author.

E-mail address: [gaetano.magnotti@kaust.edu.sa](mailto:gaetano.magnotti@kaust.edu.sa) (G. Magnotti).

[13] concentric burner. They found a slight increase in peak soot volume fraction and a decrease in luminosity with increasing OC. Zhang et al. [14] conducted a numerical and experimental study on the effects of OC in laminar ethylene flames. They used 2-color flame emission method for SVF measurement and varied OC from 21 % to 50 %. They found a rapid increase in total soot loading at higher OC and attributed this to acceleration in fuel pyrolysis caused by higher flame temperatures. Ashraf et al. [9] used point measurements to examine the effect of OC on soot and precursor nanoparticles of ethylene coflow diffusion flames. They used the Yale burner [15] and varied OC from 19 % to 40 % in an O<sub>2</sub>/N<sub>2</sub> environment. Their results showed an increase in peak centerline SVF up to 27 % OC, beyond which the peak centerline SVF began to decrease. However, their results showed an increase in precursor nanoparticles with increased OC. Several other studies have also examined the effect of OC on soot numerically [16–18] and experimentally [19–25] using other burner configurations.

While these studies are wide-ranging, they mainly utilized ethylene as fuel. Investigation of OC on sooting tendency using methane flames remains scarce, and the effect on soot precursor has barely been explored. Fewer still are soot studies of methane in O<sub>2</sub>/CO<sub>2</sub> environment relevant to oxy-combustion technologies. Moreover, most of these were carried out using the Gülder [26] or Santoro [13] type burners. The influence of burner configuration, including fuel nozzle material and diameter, on soot formation is broadly acknowledged [27].

To address this gap, the present study explores the influence of coflow OC and N<sub>2</sub> substitution on soot formation in laminar methane oxy-fuel flames in O<sub>2</sub>/CO<sub>2</sub> environment. The comparison between O<sub>2</sub>/CO<sub>2</sub> and O<sub>2</sub>/N<sub>2</sub> was done at constant adiabatic flame temperature (T<sub>ad</sub>), which can serve as the characteristic flame temperature in soot studies [28]. Planar Laser-induced Incandescence (PLII) calibrated by LEM, combined with PAH Laser Induced Fluorescence (PAH-LIF), were used to provide information on both soot and its precursor nanoparticles. Additionally, DSLR and OH\* chemiluminescence images were taken to give more details on the structure of the examined flames. For this study, we utilized a slightly modified version of our oxy-fuel burner [29–31] specifically designed for operation at high pressures. However, all the results presented in this current study were conducted at atmospheric pressures. These atmospheric cases serve as a baseline for our high-pressure soot campaigns, which will be carried out in due time.

## 2. Methodology

### 2.1. Burner and flame conditions

Fig. 1 shows a schematic of the coflow burner utilized for this study.

The burner features a central fuel jet of CH<sub>4</sub> surrounded by a coflow stream, enclosed in a quartz confinement with a square cross-section of 40 mm x 40 mm and a height of 189 mm. The inner and outer diameters of the stainless steel fuel nozzle are 1.75 mm and 3.18 mm, respectively. The burner lip thickness is 0.715 mm. The windows on both confinements are 2 mm thick and made of UV-fused silica. We opted for a square cross-section for enclosures to get lower-cost, high-quality quartz to minimize image distortions and ultimately achieve a higher spatial resolution. All the gas flow rates were controlled using Bronkhost mass flow controllers, calibrated by Drycal flow calibrator with a calibration accuracy of about  $\pm 5\%$ . The MFCs were controlled using LabVIEW and were operated between 10 % and 90 % of their full-scale capacity.

Table 1 shows the test conditions for both CO<sub>2</sub> and N<sub>2</sub> cases examined in this study. A total of ten laminar flames were examined. For all ten flames, the fuel is a CH<sub>4</sub> jet flowing at 0.88 L/min (corresponding to 6.7 m/s velocity and Re# = 670). The first five flames, dubbed CF1-5, are cases where the O<sub>2</sub> % in the oxidizer is increased by reducing the CO<sub>2</sub> flow rate. The O<sub>2</sub> flow rates were fixed at 6.15 L/min. NF1-5 flames were obtained by substituting the oxidizer CO<sub>2</sub> with N<sub>2</sub> while keeping the T<sub>ad</sub> constant. This was achieved by reducing the O<sub>2</sub>% in the oxidizer. For example, to reach the same T<sub>ad</sub> as CF3, the oxygen content of NF3 has to be reduced from 50 % to 32 % because CO<sub>2</sub> has a higher heat capacity. The O<sub>2</sub> flow rates of NF1-5 flames were also kept at 6.15 L/min while reducing the N<sub>2</sub> flow rates, leading to higher oxidizer OC. All experiments were conducted at atmospheric temperature and pressure (T = 298 K and P = 1 bar). The T<sub>ad</sub> were computed using Chemkin PRO and the GRI 3.0 kinetic mechanism.

**Table 1**  
Flame conditions examined in this study.

Flame tag	O <sub>2</sub> /CO <sub>2</sub> (%)	T <sub>ad</sub> (K)	CH <sub>4</sub> (L/min)	O <sub>2</sub> (L/min)	CO <sub>2</sub> (L/min)	O <sub>2</sub> + CO <sub>2</sub> (L/min)
CF 1	32/68	2207	0.88	6.15	13.06	19.21
CF 2	40/60	2406	0.88	6.15	9.23	15.38
CF 3	50/50	2577	0.88	6.15	6.15	12.3
CF 4	60/40	2709	0.88	6.15	4.1	10.25
CF 5	68/32	2796	0.88	6.15	2.89	9.04
Flame tag	O <sub>2</sub> /N <sub>2</sub> (%)	T <sub>ad</sub> (K)	CH <sub>4</sub> (L/min)	O <sub>2</sub> (L/min)	N <sub>2</sub> (L/min)	O <sub>2</sub> + N <sub>2</sub> (L/min)
NF 1	21/79	2216	0.88	6.15	23.14	29.29
NF 2	26/74	2423	0.88	6.15	17.5	23.65
NF 3	32/68	2579	0.88	6.15	13.06	19.21
NF 4	40/60	2709	0.88	6.15	9.32	15.47
NF 5	48/52	2798	0.88	6.15	6.67	12.82

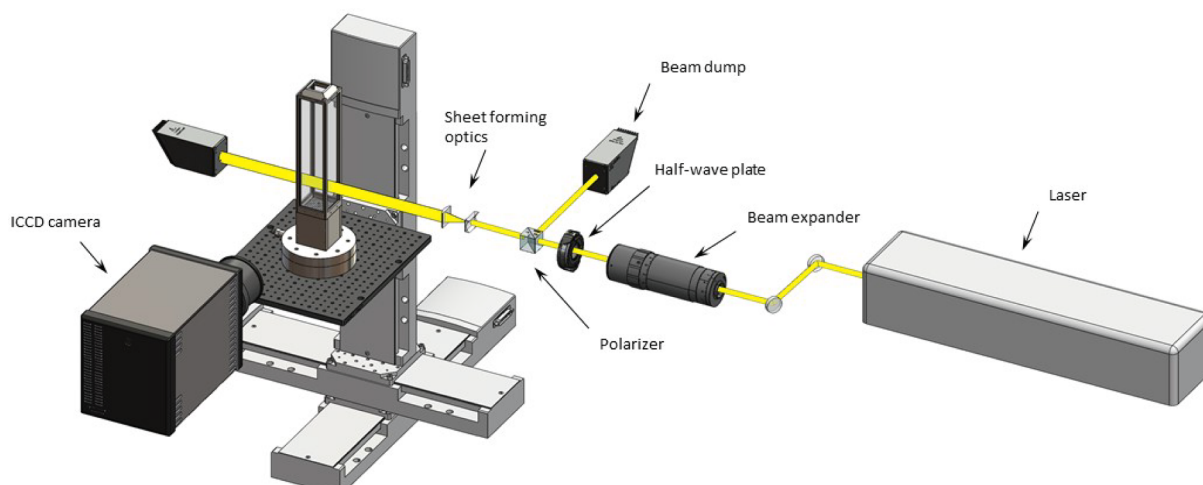


**Fig. 1.** Experimental setup for LII and LIF measurements.

## 2.2. Experimental techniques

### 2.2.1. Planar Laser-Induced Incandescence (LII)

Soot measurements were carried out using Planar Laser-Induced Incandescence calibrated by Light Extinction Method (LEM). The fundamental output (1064 nm) of a 10 Hz Q-smart 850 Quantel Nd: YAG laser was used to heat soot particles. The laser fluence was set to 0.4 J/cm<sup>2</sup> to ensure that the signal stays in the plateau region and is insensitive to minor variations in the laser energy. The curve for peak LII intensity at different laser fluences is shown in Fig. S1 of the supplementary material. A beam expander increases the beam diameter from 5 mm to 10 mm, providing a more uniform energy distribution in the central region. A half-wave plate and a polarizer allow fine tuning of laser energy delivered to the probe volume while running the laser at its maximum energy of 850 mJ. An iris placed after the polarizer blocks the edges of the laser beam. A plano-concave cylindrical lens ( $f = -100$  mm) and a plano-convex spherical lens ( $f = +400$  mm) shaped the laser into a sheet of about 50 mm height. Two razor blades were placed outside the burner to cut the edges of the laser sheet and deliver only the more uniform central 25 mm portion of the sheet to the burner. To check laser energy distribution along the 25 mm sheet, a fixed region of a stable sooting ethylene flame was exposed to different portions of the laser sheet by systematically moving the burner using a translation stage. LII signal was recorded with the assumption of constant soot concentration at a fixed height. Variations of LII signal across the the central 20 mm portion of the laser are within 9 %, and are neglected in this study. The result of this test is shown in Fig. S2 of the supplementary material.

LII signal was collected using an ICCD (PI MAX 4: 1024 by 1024) camera optimized for signal collection in the visible range. The camera was equipped with a bandpass filter of 435 nm ± 40 nm and operated with a gate delay and width of 100 ns and 50 ns, respectively. The delay was optimized for maximum signal. A total of 100 images were taken at an on-CCD accumulation of 10 to enhance SNR, at the cost of temporal resolution. Fig. S3 of the supplementary materials shows LII signal to be linear with the number of on-CCD accumulations as expected. The pixel resolution achieved for the LII images was approximately 0.06 mm/pixel.

LEM was used to correlate the LII intensity to soot volume fraction ( $f_v$ ). LII signal is proportional to  $f_v$ . To determine the calibration constant, we performed LEM and LII on the same flame and used LEM results to calibrate the LII signal.

The soot volume fraction from LEM was obtained by using the equation [32]:

$$f_v = \frac{\lambda}{6\pi E(m)} K_{ext} \quad (1)$$

where  $\lambda$  is the incident laser wavelength,  $E(m)$  is the soot absorption function, whose value has been reported to range between 0.18 and 0.42 [33], which causes uncertainties in the  $f_v$  measurements to be about ± 40 % [27]. Following previous work, we chose a constant  $E(m) = 0.37$  [34] in this study. The extinction coefficient  $K_{ext}$  can be obtained experimentally through the LEM method, by measuring the absorption of an He-Ne laser, ( $\lambda = 633$  nm) passing through a laminar ethylene flame. Using the Beer-Lambert law [35], the incident intensity ( $I_0$ ) and the transmitted intensity ( $I$ ) can be related to  $K_{ext}$  through the equation

$$\frac{I}{I_0} = e^{-K_{ext}L} \quad (2)$$

where  $L$  is the path length of the laser.  $\frac{I}{I_0}$ , also known as the transmissivity ( $\tau$ ), can be expressed as [36]:

$$\frac{I}{I_0} = \frac{T - E}{L_a - D_a} \quad (3)$$

where,  $T$  is the transmitted signal when both laser and flame are present,  $E$  is the signal recorded with flame but no laser,  $L_a$  is the signal

obtained with laser but no flame, and  $D_a$  is the signal collected in the absence of both laser and flame.

### 2.2.2. Planar Laser-Induced fluorescence (LIF)

PAH-LIF was used to obtain qualitative information on soot precursors. The fourth harmonic ( $\lambda = 266$  nm) of the Q-smart-850 laser was used as a laser source. The laser beam (5 mm diameter) was then passed through a sheet forming optics to form a 26 mm laser sheet focused at the center of the burner. To avoid LII detection, the laser energy and fluence in the PAH LIF experiments were kept low at 5.3 mJ and 25 mJ/cm<sup>2</sup>, respectively. To correct for mean energy variations along the laser sheet, the fluorescence signal from acetone molecules introduced to the burner was captured using an ICCD camera and used to normalize the PAH LIF signals. An ICCD camera (PIMAX 4, Princeton Instruments) equipped with a UV lens (LAVision VZ11-1046) was used to collect the PAH-LIF signals at 90 degrees angle. A Semrock bandpass filter (450 ± 50) was placed in front of the UV lens. Other filters (400 ± 25 nm, 400 ± 20 nm, 458 ± 10 nm) were also tested, but the resulting signal-to-noise ratio (SNR) was too low. A total of 200 images were obtained for each condition and collected with a 50 ns setting for both gate width and delay. By delaying the camera acquisition by 50 ns (delay time of 100 ns, matching the settings of the LII measurements), the signal disappears, indicating that contribution from LII are negligible. By delaying the camera acquisition by 50 ns (delay time of 100 ns, matching the settings of the LII measurements), the signal disappears, indicating that contribution from LII are negligible.

### 2.2.3. OH\* chemiluminescence

OH\* can be used as a marker for the flame front, [37], as its peak sits close to the location of maximum flame temperature. Chemiluminescence of excited OH\* radicals was recorded using the same ICCD camera and lens used for the PAH LIF experiments. A stack of two bandpass filters was used for signal collection: Semrock filter (FF02-320/40-50) with OD 7 and Edmunds 310 ± 10 nm filter with OD 4. The data was collected with a gate width of 3 ms. For the taller flames, the two different portions of the flame were imaged and stitched together to get the whole flame.

## 3. Results and Discussions

### 3.1. Visible flame appearance and flame height

Fig. 2 shows the DSLR images of the ten cases examined in this study with different OC in the coflow. The images were taken at identical camera settings (800 ISO, 1/1000 shutter speed, and f# 2.8). The CF flames (O<sub>2</sub>/CO<sub>2</sub> mixture in the oxidizer), shown in Fig. 2a, transition from taller, more luminous flames to shorter, bluer flames as OC in the oxidizer increases. A similar trend can be observed for NF flames in Fig. 2 b), although the NF flames appear brighter and larger than CF flames shown in Fig. 2 a).

Flame height ( $H_f$ ) is directly related to the flame residence time, an important parameter in soot and other pollutant formation [15].  $H_f$  is commonly defined as the distance from the burner tip to the location along the centerline where fuel and oxidizer burn stoichiometrically [38]. Experimentally,  $H_f$  can be determined by the height of the blue reaction zone [39] or by using the position of the peak centerline OH\* chemiluminescence intensity as a marker [40,41]. However, most researchers use the luminous flame height for low and moderately sooting flames with the assumption that it lies close to the stoichiometric height [32,38,39], and that was the definition used in this study. We also attempted to compare the measured flame heights from DSLR to those obtained from OH\* chemiluminescence images shown in Fig. 3. However, we were only able to compute the heights of the shorter flames because as they get taller, the OH\* signal moves from away from the flame centerline axis to the wings, complicating the  $H_f$  calculations. For

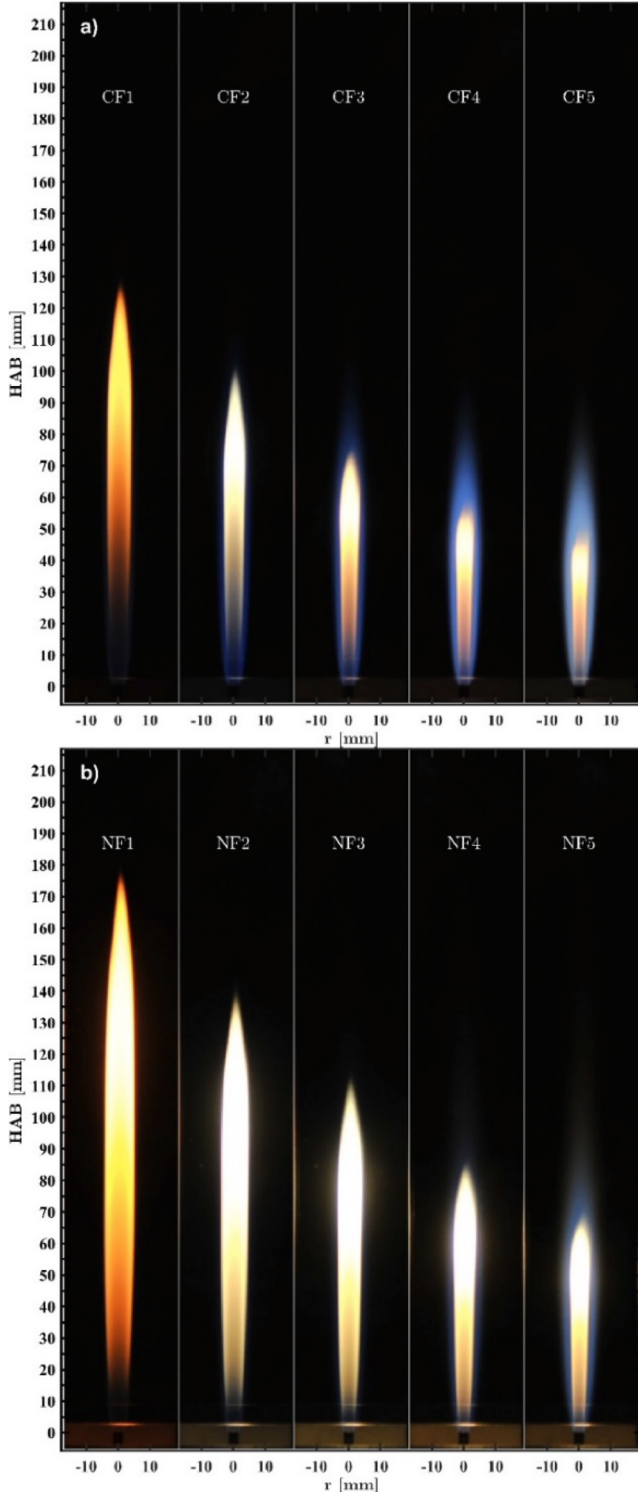


**Fig. 2.** DSLR images of (a) CF flames in  $O_2/CO_2$  oxidizer and (b) NF flames in  $O_2/N_2$  oxidizer. The OC increases from left to right for both CF and NF flames.

the cases we are able to compare, we found that  $OH^*$  heights were within 2 % of those obtained using the color images for the CF flame series. The  $OH^*$  heights were shorter by about 15 % for the sootier NF flames.

Analytical prediction of  $H_f$  in a circular port burner was first presented by the Roper correlation [42]:

$$\frac{H_f}{Q} = \frac{1}{4\pi D_0} \left(1 + \frac{1}{S}\right)^{-1} \left(\frac{T_0}{T_f}\right)^{0.67} \quad (4)$$

where  $Q$  is the volumetric flow rate of fuel;  $S$  is the stoichiometric air-to-fuel ratio;  $D_0$  is the characteristic diffusivity of the gas mixture at ambient temperature  $T_0$ ; and  $T_f$  is the characteristic temperature of mass diffusion. Roper assumed constant  $T_f = 1500K$  and  $D_0 = 20 \text{ mm}^2/\text{s}$ , which is the binary diffusion coefficient of  $O_2$  in to  $N_2$  at ambient temperature. The main drawback of this correlation lies in the assumption of constant  $T_f$  which may not be reasonable for conditions where the OC increase comes with a significant rise in  $T_{ad}$ . The increase in  $T_{ad}$  also changes the characteristic diffusivity. To account for changes in oxidizer/fuel properties, Wang et al. [43] adopted the definition for  $T_f$  proposed by Krishnan [44] earlier:

$$T_f = T_0 + \alpha(T_{ad} - T_0) \quad (5)$$

where they found the calibration constant to be  $\alpha = 0.735$ . They defined  $D_0$  as the binary diffusion coefficient of reactants ( $CH_4, O_2$ ) into products ( $CO_2, H_2O, N_2$ ) given as follows:

$$D_{react-product} = \frac{1 - X_{reac}}{\sum_{prod=1}^3 \frac{X_{prod}}{D_{react-prod}}} \quad (6)$$

where  $D_{react-product}$  represents binary diffusivity of reactant into product;  $X_{reac}$  is the reactant mole fraction, and  $X_{prod}$  is the mole fraction of products.  $D_0$  was further assumed to be the average of  $D_{CH_4-product}$  and  $D_{O_2-product}$ .

Mishra et al. [45] later used the above definition in equation (6) for  $D_0$  but replaced  $T_f$  with  $T_{ad}$ .

The variation of  $H_f$  with OC is shown in Fig. 4 a) and b). The  $H_f$  values for both NF and CF flames reduce significantly with OC. From equation (4), we observe that as OC increases, the quantity  $\left(1 + \frac{1}{S}\right)^{-1}$  becomes larger as a result, leading to increased flame heights. Additionally higher  $T_f$  caused by increased OC induces further reduction because  $T_f$  sits at the denominator of equation (4).

The figure also shows that substituting  $N_2$  with  $CO_2$  at a constant  $T_{ad}$  also leads to shorter flames. This is also related to the increased  $S$  values for NF flames. However, when  $N_2$  is substituted at constant OC (between CF1&NF3 and CF2 &NF4), the heights of CF flames are higher. At constant OC, the  $S$  values are the same, but temperature and binary diffusivity of NF flames will be higher [46], both of which are inversely proportional to flame height in equation (4).

Fig. 4 also compares our experimental flame heights with the analytical predictions of Roper [42], Mishra [45], and Wang [43] models.

While the basic formula proposed by Roper predicts the general trend of height with OC, it over-predicts the individual flame lengths of our experiments due to some of their assumptions that may not be reasonable for our flame conditions. The modifications made to  $T_f$  and  $D_0$  have improved the predicted  $H_f$ , with Mishra's matching our experiments very closely. This shows that the theoretical models developed for buoyancy-dominated flames (such as Mishras) can also reasonably predict momentum-controlled flames, as in our present study.

### 3.2. Effect of OC on soot precursor

PAHs have widely been regarded as the precursors and building blocks for soot nucleation and growth [47,48]. Planar Laser-Induced fluorescence of PAH molecules was used to obtain qualitative information on the effect of OC on precursor formation. At 266 nm excitation wavelength and using the  $450 \text{ nm} \pm 40 \text{ nm}$  filter, we prevalently target PAHs consisting of 4–5 rings [49].

Fig. 5 shows the spatial distribution of PAH LIF images of the flames

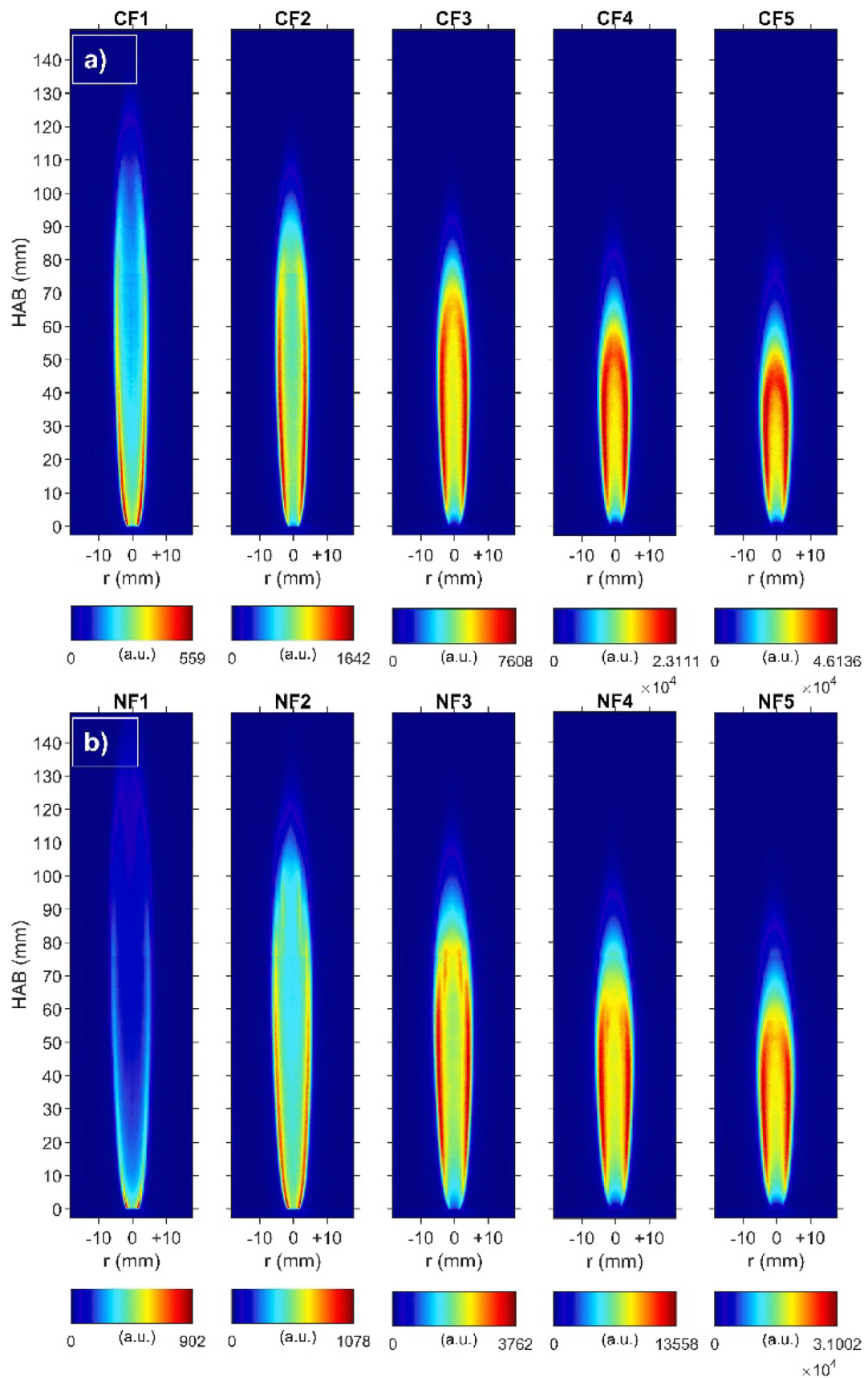


**Fig. 3.** Planar OH\* chemiluminescence images for a) CF flames and b) NF flames. The color scales for each image are different to enhance visualization in flames with low signals.

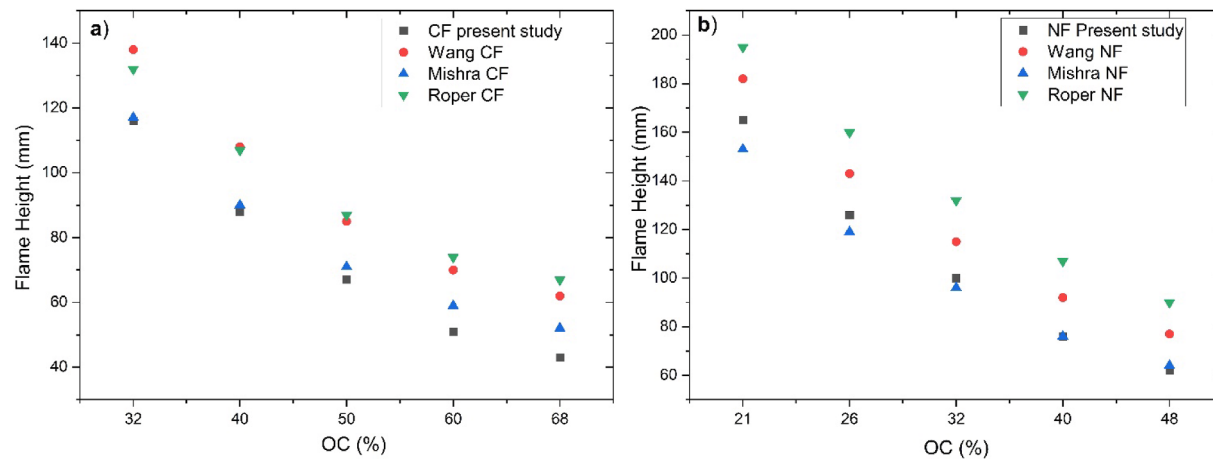


**Fig. 4.** Comparison of experimental and predicted flame heights(wang[43], Mishra[45], Roper[42]) for (a) CF flames (b) NF flames.

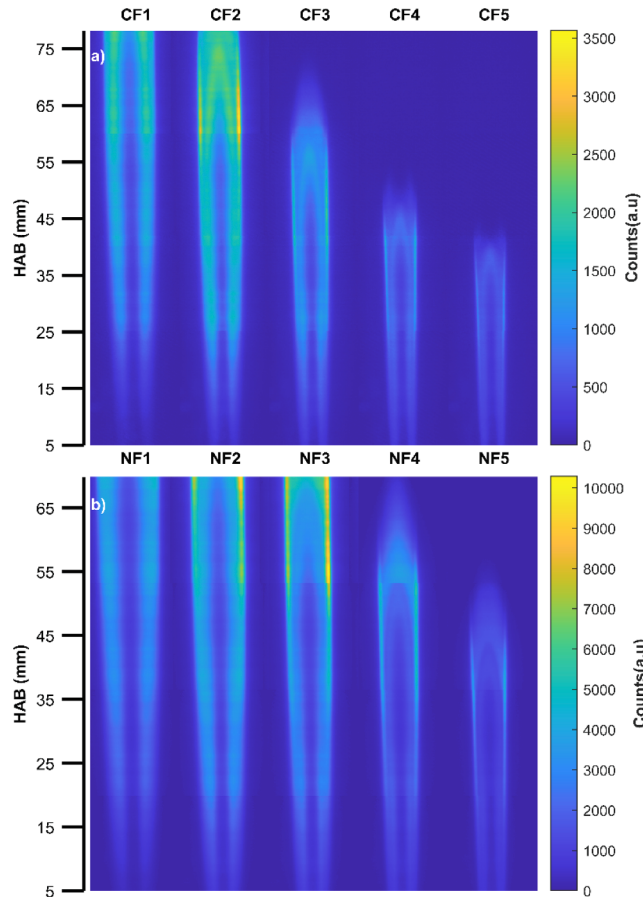


**Fig. 5.** PAH LIF signal distribution for (a) CF flames and (b) NF flames.

examined in this study. Each image is a composite of data taken at four different heights and stitched together after background subtraction and laser energy normalization. The asymmetrical distribution of the PAH signal is likely caused by energy attenuation as the laser passes through the flame.

To quantify the effect of OC on PAH formation, the peak intensities of PAH signal  $HAB/H_f = 0.5$  are shown in Fig. 6. Normalized height was chosen to account for the variation of flame length between the various flames.

In both  $O_2/CO_2$  and  $O_2/N_2$  environments, increasing OC increases the PAH LIF signal up to a certain point beyond which it decreases

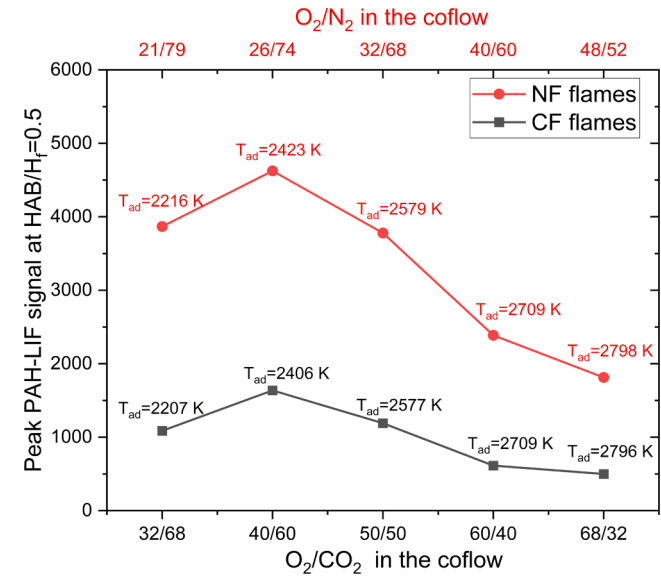


**Fig. 6.** Peak PAH-LIF signal for CF and NF flames at  $HAB/H_f = 0.5$ .

rapidly. Moreover, this reversal in behavior occurs at the same  $T_{ad}$  for both environments. This indicates that temperature is perhaps the main driving force behind this trend reversal, more than chemistry. We posit that the  $T_{ad}$  increase with OC initially favors the formation of soot precursors but, at higher temperatures, begins to have inhibiting tendencies. This conclusion is supported by a numerical study by Tao [50] in a 1-D plug flow reactor where they report mole fractions of PAHs of various sizes peaking at a particular temperature value beyond which they decrease. It should be noted that temperature-induced quenching might contribute to the diminished PAH signals observed at higher OC [41].

Fig. 6 also shows a significantly higher PAH concentration when  $CO_2$  is replaced by  $N_2$  at constant  $T_{ad}$ . This is likely a result of the chemical suppression of PAH by  $CO_2$ , which causes decreased concentrations of reactive species such as propargyl, an important radical in the formation of PAHs [48].

### 3.3. Soot volume fraction

Fig. 7 (a) and (b) show the planar distribution of soot volume fraction for the CF and NF series. The images result from vertical concatenation of data taken at 12 axial heights of each flame. Due to the limitation of

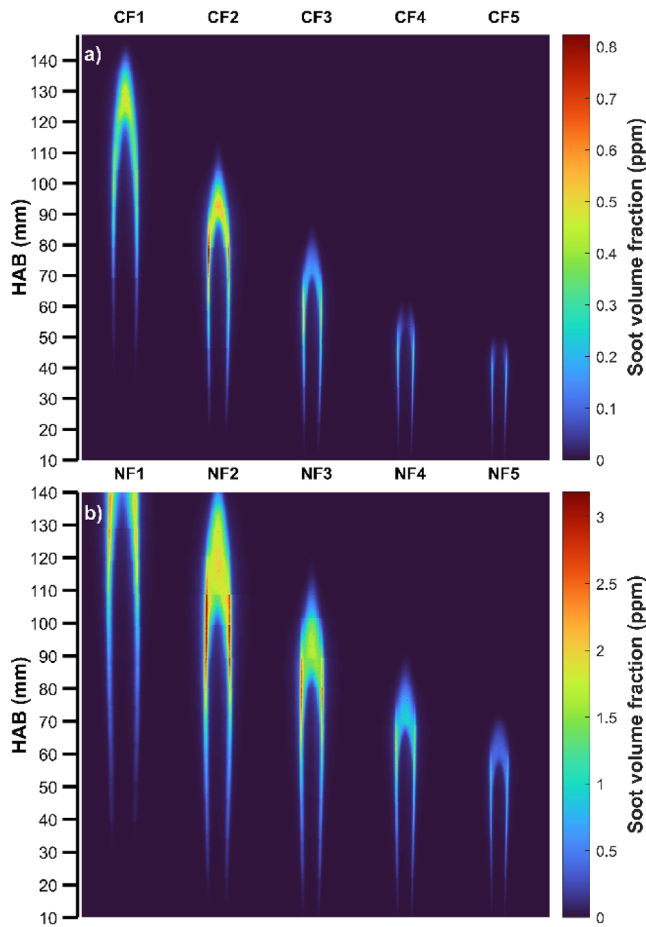


**Fig. 7.** Soot Volume Fraction of (a) CF and (b) NF methane flames.

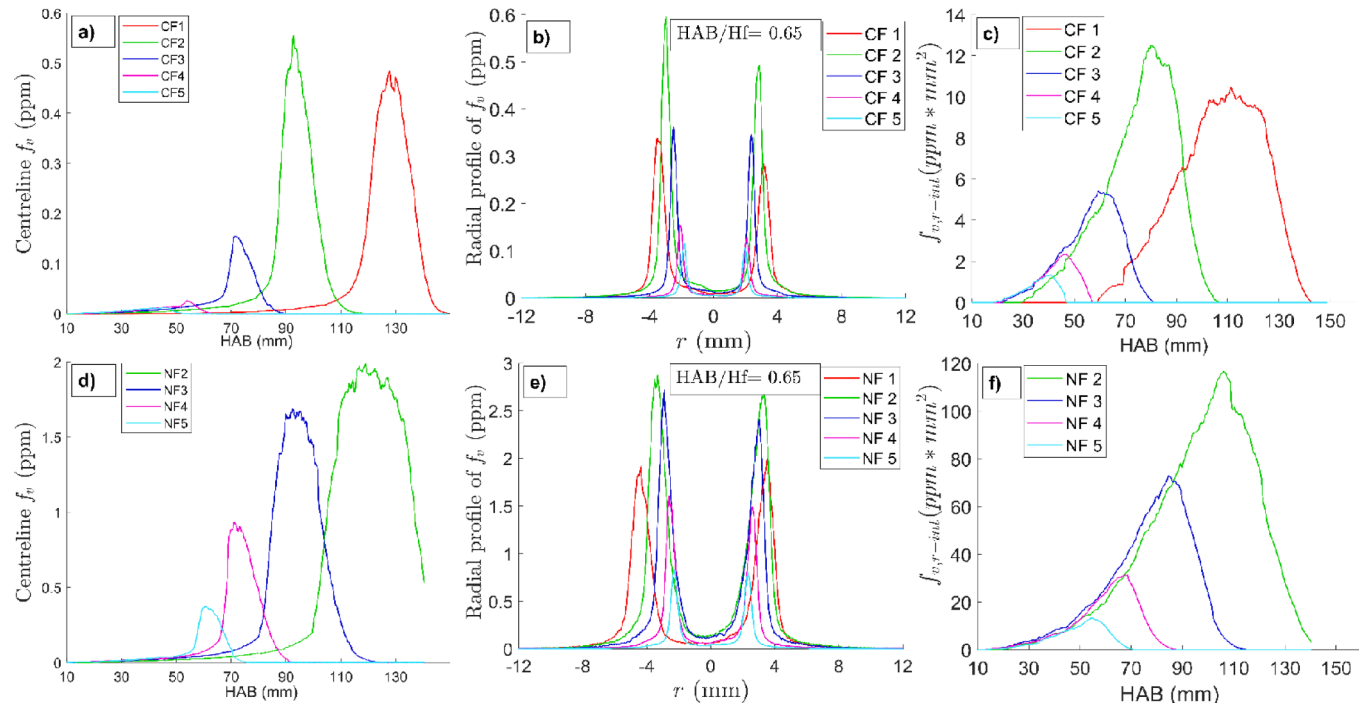
our experimental setup, we could only probe about 75 % of the luminous flame height for the NF1 case. Fig. 7 a) shows a significant effect of OC on both the soot height and the flame structure. As expected, the soot height decreases, as does the width of the soot region, as OC increases. However, the soot distribution shifts gradually from the center to the flame wings at higher OCs, and at 68 % OC, the flame wing is almost entirely separated from the central tip. The OH\* images in Fig. 3 show the opposite behavior of the LII soot images, where we see a more intense high-temperature zone at the center of the oxygen-rich flames, inciting a rapid soot oxidation in those regions [12,14]. The NF flame series shows a similar inverse relation between the OH\* signal and the soot volume fraction, as shown in Fig. 7 b). For both series, Fig. 7 shows that the position of soot inception moves closer to the fuel tube with increased OC, a trend consistent with earlier observations [12,51].

Fig. 8 shows the centerline and radially integrated profiles of  $f_v$ , in addition to the radial profile of all flames at HAB/H<sub>f</sub> = 0.65. The centerline and radially integrated profiles of NF1 flame are not shown due to the lack of completeness of the data, as explained earlier.

Fig. 8 (a) show an increase (CF1-2) and then a decrease (CF2-5) in the centreline peak  $f_v$  with increasing OC. A similar trend of decrease in centerline peak (NF2-5) is observed for NF cases, as shown in Fig. 8 d). The centreline peak  $f_v$  are also consistently higher for the NF cases, in addition to having broader profiles.

Fig. 8 (b) and (e) show the radial profiles of CF and NF flames obtained at a normalized height of HAB/H<sub>f</sub> = 0.65. The figures show that an OC increase initially results in higher radial peaks, which decrease after CF2/NF2 is reached. The same trend is observed for other normalized heights, but only results at HAB/H<sub>f</sub> = 0.65 are shown for brevity. Fig. 8 (b) and (e) also show slight asymmetries in the left and right profiles, which are likely caused by the attenuation of laser energy as it passes through the flame. These asymmetries are more noticeable for the sootier flames. Comparing the CF and NF profiles, the NF cases have broader profiles and considerably higher radial peak  $f_v$ , pointing to higher soot production.

Fig. 8 (c) and (f) show radially integrated  $f_v$ . This term is defined [52] as



**Fig. 8.** (a) centreline profiles of  $f_v$  for CF flames (b) radially integrated  $f_v$  for CF flames (c) Radial profiles at HAB/H<sub>f</sub> = 0.65 for CF flames (d) Centreline profiles of  $f_v$  for NF flames e) radially integrated  $f_v$  for NF flames (f) Radial profiles at HAB/H<sub>f</sub> = 0.65 for NF flames.

$$f_{v,r-int} = 2\pi \int_0^R f_v(r, h) r dr \quad (7)$$

where R is the radial distance between the centerline and the boundary of the sooting region. To minimize the effect of noise, we set the location of 5 % of the maximum to determine the soot region boundary and only half of the flame on the laser side was used. Fig. 8 c) and f) presents the  $f_{v,r-int}$  for both series of flames. Fig. 8 c) shows the peak  $f_{v,r-int}$  increased by almost 20 % with OC going from CF1 to CF2, decreasing precipitously afterward. A similar drop in peak  $f_{v,r-int}$  is observed for NF2-5 flames, as shown in Fig. 8 f). The magnitudes of the  $f_{v,r-int}$  are an order of magnitude higher for the NF cases than the CF cases through the combined effect of higher peak  $f_v$  and broader soot layer thickness for the NF cases.

The slopes of the radially integrated profiles,  $\frac{df_{v,r-int}}{dh}$  are plotted in Fig. 9 to characterize the evolution of soot (where h stands for the HAB). As explained by Qi et al. [53], this parameter can be used to compare the rates of soot formation ( $\frac{df_{v,r-int}}{dh} > 0$ ) and oxidation ( $\frac{df_{v,r-int}}{dh} < 0$ ) when the fuel flow rates of all conditions are kept constant (which is the case for all our flames). Fig. 9 shows an increase in  $\frac{df_{v,r-int}}{dh}$  between CF1-2 followed by a decrease from CF2-5 (similarly for NF2-5). The figure also shows soot is formed and oxidized at faster rates for NF flames than for the CF flames, indicating that substituting CO<sub>2</sub> with N<sub>2</sub> in the oxidizer leads to higher rates of soot formation.

Fig. 10 a) shows the peak soot volume fraction and Fig. 10 b) the volumetrically integrated soot volume fractions indicative of the flame's total soot loading, accounting for the differences in size and volume. As stated by Zelepuoga [47] and others [12,51], the volumetrically integrated soot volume fraction is computed from equation (8), where H represents the height of the flame. Only the laser side of the flame was used for volumetrically integrated soot volume fraction calculations to avoid LII signal attenuation problems mentioned earlier.

$$f_{v,vol-int} = \int_0^H dh \int_0^R 2\pi f_v(r, h) r dr \quad (8)$$

Fig. 10 a) shows a slight increase in soot loading as OC increased from 32 % to 40 %, beyond which the  $f_{v,vol-int}$  begins to decrease. This increase in soot loading between 32 % and 40 % OC occurs despite the shorter  $H_f$  (and hence smaller residence time) of the case with 40 % OC. The NF curve (in red) shows almost 17x reduction in the  $f_{v,vol-int}$  as OC goes from 26 % to 48 %, which is smaller than the 22x reduction after the reversal point for the CF cases. This indicates a relatively higher temperature sensitivity of soot loading in O<sub>2</sub>/CO<sub>2</sub> compared to O<sub>2</sub>/N<sub>2</sub> environments. The figure also shows that the total soot loadings for NF flames are higher than those for CF cases, and the gap between them shrinks at higher OC.

Fig. 10 (b) shows the peak  $f_v$  values ( $f_{v,max}$ ) obtained by averaging the top 5 signals in each flame. The averages of the top 10 and 20 signals were also taken, but they differ from the mean of the top 5 signals by less than 2 %. With increasing OC,  $f_{v,max}$  reaches a maximum and then decreases almost linearly after a certain OC (26 % for CF and 40 % for NF). This closely follows the evolution of PAHs, as seen in section 3.2. Interestingly, the trend reversal for the soot also happens at the same OC as those of the PAHs. This further shows the importance of these 4–5 rings PAHs in dictating the soot formation processes of laminar diffusion flames.

Jain. et al. [16] report  $f_{v,max}$  values for in CH<sub>4</sub> flames in O<sub>2</sub>-enriched air using 2-color pyrometry technique. They found that between OC range from 21 %–76.3 %, the  $f_{v,max}$  peaks at OC of about 36 %, beyond which it decreases monotonically, a behavior also captured by their numerical simulation. They attributed this phenomenon to competing effects of higher temperature and reduced residence time (which allows less time for soot production), with the latter having more preponderance over the former at higher OC.

Ashraf et al. [9] report a reversal OC to be 27 % in C<sub>2</sub>H<sub>4</sub> flames in O<sub>2</sub>/N<sub>2</sub> atmosphere. They gave a similar explanation as that offered by Jain to explain this phenomenon. Interestingly, the reversal OC and T<sub>ad</sub> reported by Ashraf et al. is similar to our results in O<sub>2</sub>/N<sub>2</sub> environment despite the differences in flame conditions, burner configuration, and fuel type. This further supports the idea that temperature plays a crucial role in this behavior, more so than chemistry. However, this trend reversal may not always be observed when considering a narrower range OC. For example, Fuentes [18] (OC of 21–35 % in C<sub>2</sub>H<sub>4</sub>) and Escudero [52] (OC of 21–37 % in C<sub>2</sub>H<sub>4</sub>, C<sub>3</sub>H<sub>8</sub>, and C<sub>4</sub>H<sub>10</sub>) both report an increase in  $f_{v,max}$  over the entire range of the OC they considered.

Fig. 10 b) shows that when N<sub>2</sub> is substituted for CO<sub>2</sub> at fixed OC (as shown for 32 % and 40 % OC), we also see a reduction in  $f_{v,max}$  for the CO<sub>2</sub> cases. This result is consistent with several studies [19,20,54–59], showing that CO<sub>2</sub> addition disrupts the soot formation in hydrocarbon flames due to thermal and chemical effects. The thermal contribution comes mainly from the reduction in flame temperature induced by CO<sub>2</sub> owing to its relatively high molar-specific heat capacity [57]. We see an almost 5x reduction in  $f_{v,max}$  at 32 % (between CF1 & NF3) and 2x reduction at 40 % OC (between CF2 & NF4) in O<sub>2</sub>/CO<sub>2</sub> compared to O<sub>2</sub>/N<sub>2</sub> environment. This shrinkage in the gap can be attributed to the non-linear effect of temperature on soot and its precursors, suggesting that at higher temperatures, chemistry is more responsible for the difference in  $f_{v,max}$  than temperature.

Fig. 10 (b) also shows significantly higher (4 to 5 times)  $f_{v,max}$  for the NF cases when CO<sub>2</sub> is replaced with N<sub>2</sub> constant T<sub>ad</sub>. The OC had to be slightly reduced for the NF cases to fix the T<sub>ad</sub> between the NF and CF. We attribute this to reduced residence times of CF flames (as indicated by the  $H_f$  measurements) and chemical suppression of soot by CO<sub>2</sub> [19,20,54–59].

Lui et al. [19] identified the reaction CO<sub>2</sub> + H  $\rightleftharpoons$  CO + OH as the main driver behind the chemical suppression of soot by CO<sub>2</sub> dilution. The higher consumption rates of H radicals (which play an active role in surface growth [60]), coupled with increased concentrations of OH radicals with CO<sub>2</sub> addition, lead to the suppression of soot precursors and nascent soot. This explanation is supported by our peak OH\* chemiluminescence intensities shown in Fig. 11 a). The figure shows consistently higher values of peak OH\* signal for CF cases when T<sub>ad</sub> is kept constant.

However, the OH\* intensity may not always correlate to the concentration of ground-state OH radical concentration [61]. Hence, we plot the OH concentration predicted from 1D opposed-flow flame calculations using Chemkin PRO and GRI 3.0 mechanism in Fig. 11 b). The simulation result likewise shows higher OH radical intensities for CF cases than NF cases.

Another useful parameter for the quantification of the sooting tendency in flames is the soot yield ( $Y_s$ ), which represents the percentage of carbon mass in the fuel converted to soot [62–64]. It is defined as:

$$Y_s = \frac{\dot{m}_s(h)}{\dot{m}_c} \quad (9)$$

where the mass flow rate of carbon turned into soot ( $\dot{m}_s(h)$ ) can be expressed as:

$$\dot{m}_s(h) = v_h(h) \rho_s \int 2\pi r f_v(r, h) dr \quad (10)$$

Soot density ( $\rho_s$ ) is usually taken to be 1.8 g/cm<sup>3</sup> [11,62]. The axial velocity is given by the formula  $v_h(h) = \sqrt{2ah}$ , where the acceleration due to thermal buoyancy ( $a$ ) is commonly taken to be 25 m/s<sup>2</sup> for laminar flame studies [51,63,65–67]. The mass flow rate of carbon at the burner fuel tube ( $\dot{m}_c$ ) in this study is a kept constant at 8.25 mg/s.

As shown in Fig. 12, the location of peak carbon conversion is moved further downstream at higher OCs, as is the case for the centerline and radially integrated profiles. The maximum percentage of carbon conversion to soot ( $Y_{s,max}$ ) are shown in Fig. 13. As expected,  $Y_{s,max}$  for the

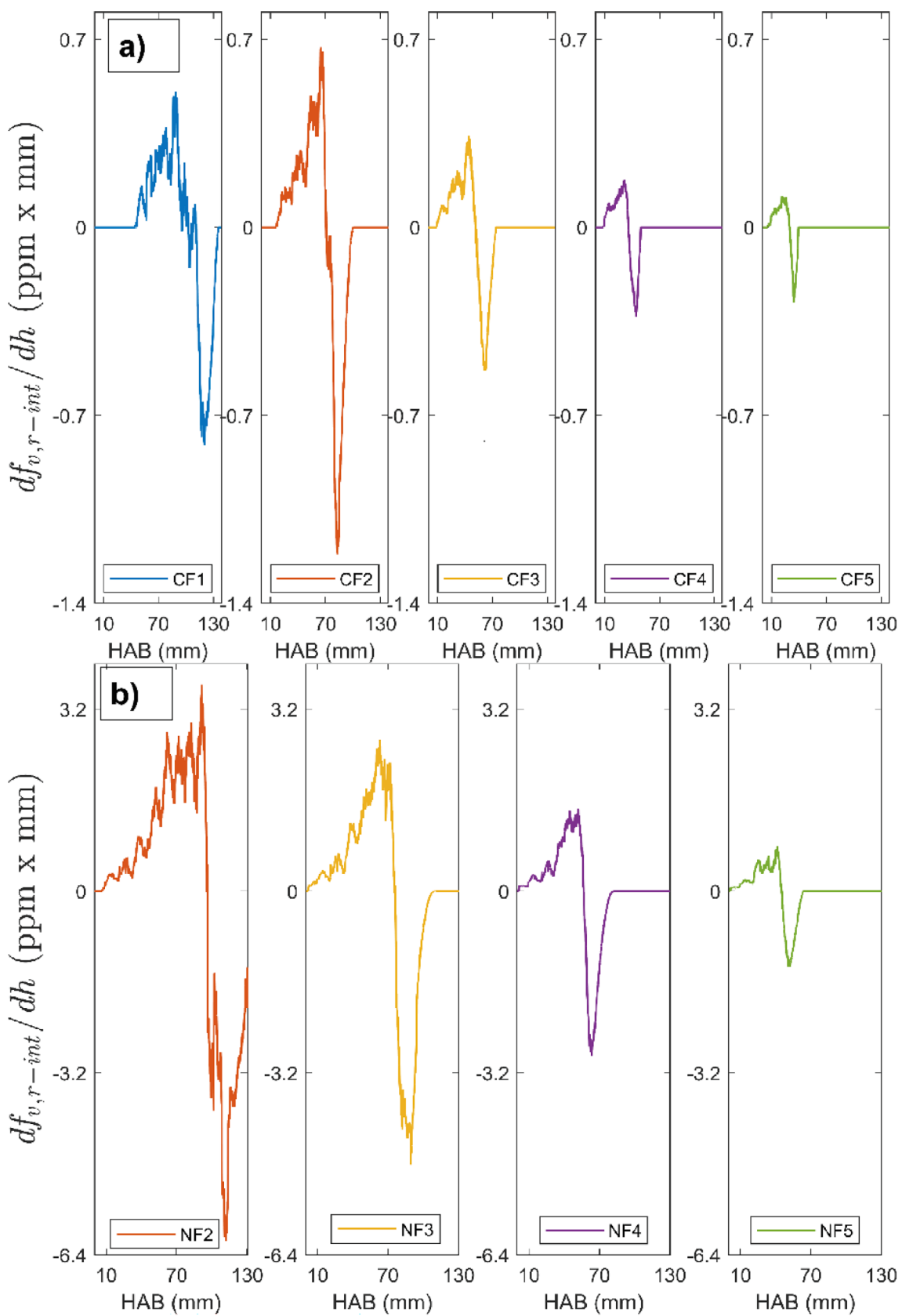


**Fig. 9.** Rates of soot formation and oxidation for (a) CF flames and (b) NF flames.

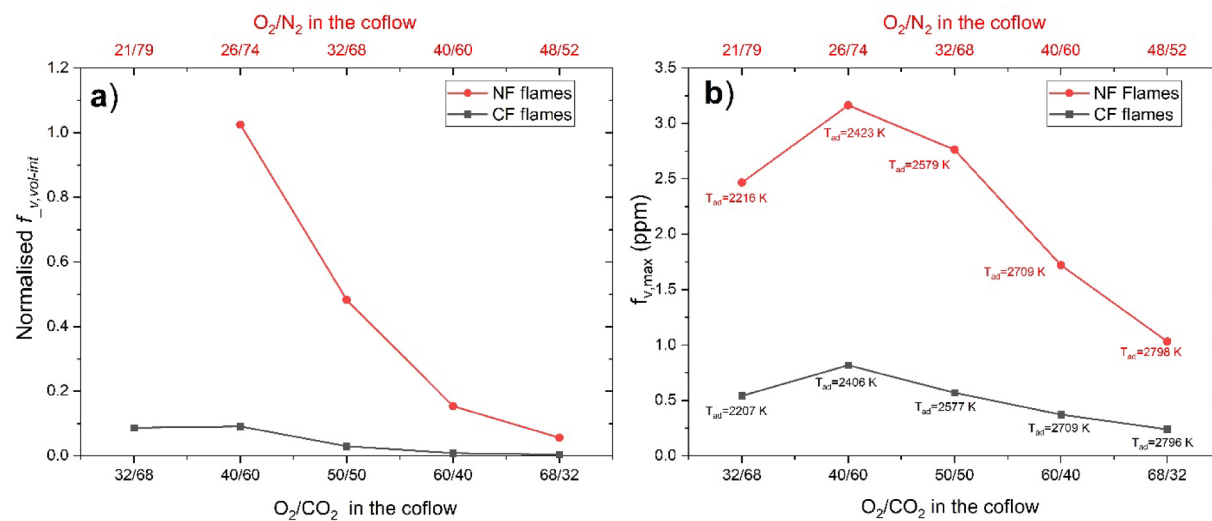


**Fig. 10.** (a) volumetrically integrated soot volume fraction for cf and nf flames normalized by the value for nf2 (i.e., maximum value) (b) Peak soot volume fraction for all CF and NF flames.

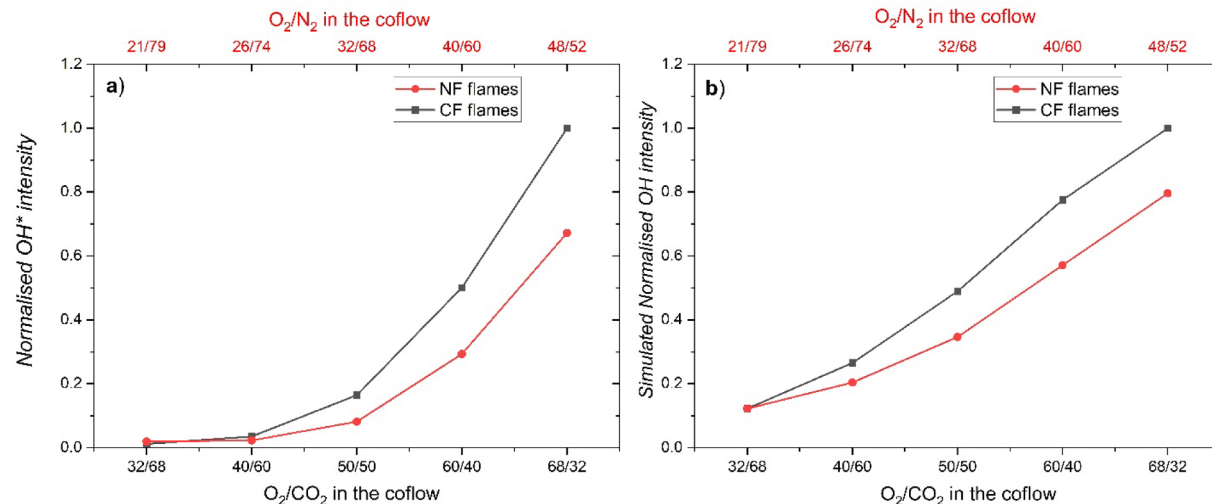


**Fig. 11.** A) peak  $\text{OH}^*$  intensity normalized by the maximum value for all cf and nf flames b) normalised peak oh mole fraction obtained from 1-d chemkin calculation opposed flow calculation.

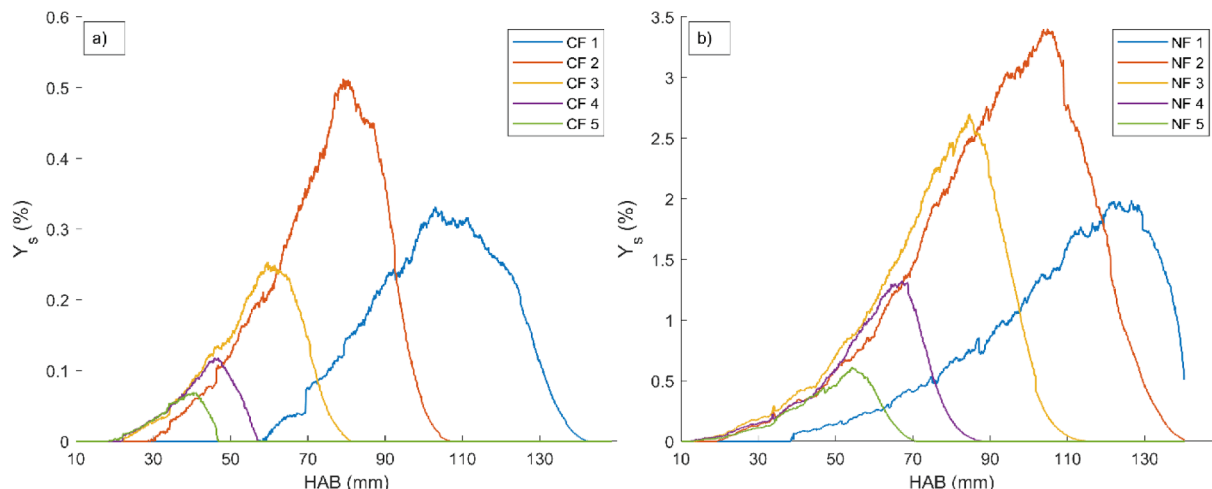


**Fig. 12.** Plots soot yield at various HAB for (a) CF flames, (b) NF flames.

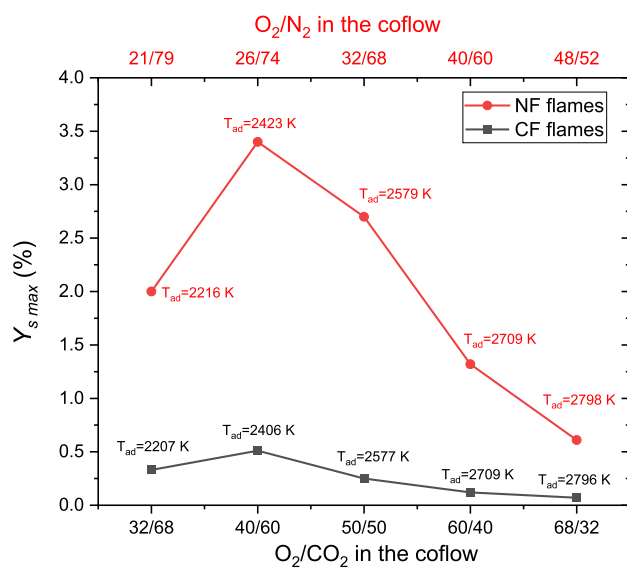


**Fig. 13.** Plot of maximum soot yield for CF and NF flames. Note: Because the black curve appears compressed due to the scale, it is plotted separately on a different scale in Fig. S4 of supplementary material for better visibility of the trend.

flame in O<sub>2</sub>/N<sub>2</sub> are significantly higher than those in O<sub>2</sub>/CO<sub>2</sub> at constant T<sub>ad</sub>. Furthermore, the basic reversal trend observed for other soot parameters at 40 % OC (for CF) and 26 % OC (for NF) are also present in Y<sub>s,max</sub> curves. This result contradicts the findings from prior studies by He et al. [68] and Zhang et al. [51], in which they report a positive linear relationship between Y<sub>s,max</sub> and T<sub>ad</sub> for C<sub>3</sub>H<sub>8</sub>, C<sub>2</sub>H<sub>6</sub>, CH<sub>4</sub> and n-heptane flames burning in O<sub>2</sub>/N<sub>2</sub> environments. This discrepancy can be explained by noting the limited T<sub>ad</sub> range of the flames studied (about 2100 K – 2400 K), which lies left of the vertex point shown in Fig. 13. We believe that by examining a higher range of T<sub>ad</sub>, they may also observe the point at which they curve turns and slope turns negative.

#### 4. Conclusion

The effects of O<sub>2</sub>/CO<sub>2</sub> and O<sub>2</sub>/N<sub>2</sub> on flame height, flame structure, soot, and PAHs were investigated for laminar CH<sub>4</sub> oxy-fuel flames at atmospheric pressure using non-intrusive experimental techniques. The fuel conditions were kept constant for all the ten flames we studied. The following are some of the findings obtained from the study:

- The visual flame height decreases monotonically as oxidizer oxygen concentration increases. The three theoretical models capture the trend of experimental height. However, they overpredict the magnitudes, with Mishra's correlation coming closest to our results, proving that correlations developed for buoyancy-dominated flames can also reasonably predict flame height in momentum-dominated flames.
- The soot distribution showed earlier soot inception with increased OC. The maximum soot volume fraction location moves from the centerline to the wings as OC increases. The OH\* images show the opposite trend as the soot images point to the enhancements of oxidative processes in the high-temperature regions of the flame.
- The concentration of PAH increased with OC and then began to decrease at 40 % and 26 % OC for O<sub>2</sub>/CO<sub>2</sub> and O<sub>2</sub>/N<sub>2</sub> flames, respectively. This behavior is reflected across multiple soot-assessing parameters, including the peak radially integrated soot volume fraction and the flame-wide peak soot volume fraction. It was explained that the increase in T<sub>ad</sub>, caused by the increase in OC, is mainly responsible for causing the trend reversal through its non-

linear effect on soot precursors PAHs. These results further underscore the importance of T<sub>ad</sub> in dictating sooting behavior.

- Flames burning in O<sub>2</sub>/N<sub>2</sub> environment at constant T<sub>ad</sub> displayed a consistently higher sooting propensity than O<sub>2</sub>/CO<sub>2</sub> cases due to the combined effect of reduced residence time and chemical effect.
- Furthermore, the total percentage of carbon mass converted to soot was observed also to follow this trend reversal with T<sub>ad</sub>. Our results contradicted some studies that reported a linear positive relationship between maximum soot yield and T<sub>ad</sub>. It was explained that was likely due to the limitation in the range of T<sub>ad</sub> they looked at.

These results can serve as helpful baseline cases to probe the relative effect of pressure on sooting propensity in O<sub>2</sub>/CO<sub>2</sub> vs O<sub>2</sub>/N<sub>2</sub> environment, which we plan to conduct in subsequent studies.

#### CRediT authorship contribution statement

**Muhammad Bukar:** Conceptualization, Formal analysis, Investigation, Methodology, Software, Visualization, Writing – original draft. **Suman Basnet:** Software, Visualization, Investigation. **Peng Liu:** Investigation, Writing – review & editing. **Gaetano Magnotti:** Funding acquisition, Project administration, Supervision, Writing – review & editing, Conceptualization.

#### Declaration of competing interest

The authors declare that they have no known competing financial interests or personal relationships that could have appeared to influence the work reported in this paper.

#### Acknowledgment

This work was funded entirely by the King Abdullah University of Science and Technology, Saudi Arabia.

#### Appendix A. Supplementary data

Supplementary data to this article can be found online at <https://doi.org/10.1016/j.fuel.2025.134291>.

#### Data availability

Data will be made available on request.

#### References

- Nemitallah MA, Habib MA, Badr HM, Said SA, Jamal A, Ben-Mansour R, et al. Int J Energy Res 2017;41(12):1670–708.
- Markewitz P, Kuckshinrichs W, Leitner W, Linssen J, Zapp P, Bongartz R, et al. Energy Environ Sci 2012;5(6):7281–305.
- Lighty JS, Veranth JM, Sarofim AF. J Air Waste Manag Assoc 2000;50(9): 1565–618.
- Kumfer B, Kennedy I, editors. The role of soot in the health effects of inhaled airborne particles. Combustion generated fine carbonaceous particles, in: Proceedings of an International Workshop held in Villa Orlandi, Karlsruhe University Press, Anacapri; 2009.
- Kerr RA. Soot is warming the world even more than thought. American Association for the Advancement of Science 2013.
- Sammak M, Thern M, Genrup M, editors. Performance of a Semi-Closed Oxy-Fuel Combustion Combined Cycle (SCOC-CC) With an Air Separation Unit (ASU). Turbo Expo: Power for Land, Sea, and Air; 2018: American Society of Mechanical Engineers.
- Allam R, Martin S, Forrest B, Fetvedt J, Lu X, Freed D, et al. Energy Procedia 2017; 114:5948–66.
- Claramunt K, Consul R, Carbonell D, Pérez-Segarra C. Combust Flame 2006;145(4): 845–62.
- Ashraf M, Ahmed H, Steinmetz S, Dunn M, Masri A. Fuel 2021;300:120913.
- Gilder ÖL. Combust Flame 1995;101(3):302–10.
- Lee K-O, Megaridis CM, Zelepouga S, Saveliev AV, Kennedy LA, Charon O, et al. Combust Flame 2000;121(1–2):323–33.
- Sun Z, Dally B, Alwahabi Z, Nathan G. Combust Flame 2020;211:96–111.
- Santoro R, Semerjian H, Dobbins RA. Combust Flame 1983;51:203–18.

- [14] Zhang Y, Liu F, Lou C. *Energy Fuels* 2018;32(5):6252–63.
- [15] Smooke M, Long M, Connolly B, Colket M, Hall R. *Combust Flame* 2005;143(4): 613–28.
- [16] Jain A, Das DD, McEnally CS, Pfefferle LD, Xuan Y. *Proc Combust Inst* 2019;37(1): 859–67.
- [17] Xu L, Yan F, Zhou M, Wang Y, Chung SH. *Combust Flame* 2018;197:304–18.
- [18] Fuentes A, Henríquez R, Nmira F, Liu F, Consalvi J-L. *Combust Flame* 2013;160(4): 786–95.
- [19] Liu F, Guo H, Smallwood GJ, Gülder ÖL. *Combust Flame* 2001;125(1–2):778–87.
- [20] Kailasanathan RKA, Yelverton TL, Fang T, Roberts WL. *Combust Flame* 2013;160 (3):656–70.
- [21] Oh KC, Shin HD. *Fuel* 2006;85(5–6):615–24.
- [22] Shaddix CR, Williams TC. *Proc Combust Inst* 2017;36(3):4051–9.
- [23] Escudero F, Fuentes A, Demarco R, Consalvi J-L, Liu F, Elicer-Cortés J, et al. *Exp Therm Fluid Sci* 2016;73:101–8.
- [24] Liu P, Chu C, Alsheikh I, Gubba SR, Saxena S, Chatakonda O, et al. *Combust Flame* 2022;245:112378.
- [25] Wang Q, Legros G, Bonnety J, Morin C, Matynia A, Consalvi J-L, et al. *Combust Flame* 2017;183:242–52.
- [26] Gülder ÖL, Snelling DR. *Combust Flame* 1993;92(1–2):115–24.
- [27] Zhang Z, Zhou L, He X. Applications in Energy and Combustion. *Science* 2023;13: 100103.
- [28] Axelbaum R, Law CK, editors. Soot formation and inert addition in diffusion flames. *Symposium (International) on Combustion*; 1991: Elsevier.
- [29] Kim T, Bukar M, Basnet S, Magnotti G. *Fuel* 2024;371:132114.
- [30] Bukar M, Basnet S, Wu B, Magnotti G, editors. An Experimental Study of the Stability and Nearfield Structure of Oxyfuel Jet Flames at Elevated Pressures. *Turbo Expo: Power for Land, Seaand Air*. American Society of Mechanical Engineers; 2023.
- [31] Bukar M, Basnet S, Kim T, Magnotti G, editors. Effect of O<sub>2</sub>/CO<sub>2</sub> ratio on stability and near field structure of oxyfuel jet diffusion flames at atmospheric pressure. *AIAA SCITECH 2022 Forum*; 2022.
- [32] Bennett AM, Liu P, Li Z, Kharbatia NM, Boyette W, Masri AR, et al. *Combust Flame* 2020;220:210–8.
- [33] Hadwin PJ, Sipkens T, Thomson K, Liu F, Daun K. *Appl Phys B* 2016;122:1–16.
- [34] Boyette WR, Bennett AM, Cenker E, Guiberti TF, Roberts WL. *Combust Flame* 2021; 227:271–82.
- [35] Zhao H, Ladommato N. *Prog Energy Combust Sci* 1998;24(3):221–55.
- [36] Gupta N, Sankaranarayanan A, Sasidharakurup R, Chowdhury A, Kumbhakarna N. *J Aerosol Sci* 2021;155:105773.
- [37] Marchese A, Dryer F, Nayagam V, Colantonio R, editors. Hydroxyl radical chemiluminescence imaging and the structure of microgravity droplet flames. *Symposium (International) on Combustion*; 1996: Elsevier.
- [38] Mitchell RE, Sarofim AF, Clomberg L. *Combust Flame* 1980;37:227–44.
- [39] Gordon A, Li S, Williams F. *Combust Sci Technol* 1999;141(1–6):1–18.
- [40] Liu P, Zhang Y, Guo J, Alfazazi A, Chu C, Serrano-Bayona R, et al. *Proc Combust Inst* 2024;40(1–4):105215.
- [41] Liu P, Guo J, Im HG, Roberts WL. *Combust Flame* 2023;258:112379.
- [42] Roper F. *Combust Flame* 1977;29:219–26.
- [43] Wang Z, Sunderland PB, Axelbaum RL. *Proc Combust Inst* 2019;37(2):1547–53.
- [44] Krishnan S, Abshire J, Sunderland P, Yuan Z-G, Gore J. *Combust Theor Model* 2008;12(4):605–20.
- [45] Mishra A, Sharma P, Gebreyesus BY, Kumar M, Ray A. *Combust Sci Technol* 2024; 196(2):223–44.
- [46] Mikofski MA, Williams TC, Shaddix CR, Blevins LG. *Combust Flame* 2006;146 (1–2):63–72.
- [47] Zelepouga SA, Saveliev AV, Kennedy LA, Fridman AA. *Combust Flame* 2000;122 (1–2):76–89.
- [48] Zhang Y, Wang L, Liu P, Guan B, Ni H, Huang Z, et al. *Combust Flame* 2018;192: 439–51.
- [49] Liu P, He Z, Hou G-L, Guan B, Lin H, Huang Z. *Chem A Eur J* 2015;119(52): 13009–17.
- [50] Tao H, Wang H-Y, Ren W, Lin KC. *Fuel* 2019;255:115796.
- [51] Zhang Z, Zhou L, He X, Chen L, Wei H. *Combust Flame* 2023;251:112719.
- [52] Escudero F, Fuentes A, Consalvi J-L, Liu F, Demarco R. *Fuel* 2016;183:668–79.
- [53] Qi S, Sun Z, Wang Z, Liu Y, He Y, Liu S, et al. *Proc Combust Inst* 2021;38(1): 1225–32.
- [54] Karataş AE, Gülder ÖL. *Fuel* 2017;200:76–80.
- [55] Min J, Baillot F, Guo H, Domingues E, Talbaut M, Patte-Rouland B. *Proc Combust Inst* 2011;33(1):1071–8.
- [56] Mortazavi H, Wang Y, Ma Z, Zhang Y. *Exp Therm Fluid Sci* 2018;92:97–102.
- [57] Schug K, Manheimer-Timnat Y, Yaccarino P, Glassman I. *Combust Sci Technol* 1980;22(5–6):235–50.
- [58] McLintock IS. *Combust Flame* 1968;12(3):217–25.
- [59] Guo H, Smallwood GJ. *Combust Sci Technol* 2008;180(10–11):1695–708.
- [60] Du D, Axelbaum R, Law CK, editors. The influence of carbon dioxide and oxygen as additives on soot formation in diffusion flames. *Symposium (international) on Combustion*; 1991: Elsevier.
- [61] Hall JM, Petersen EL. *Int J Chem Kinet* 2006;38(12):714–24.
- [62] Liu F, Karataş AE, Gülder ÖL, Gu M. *Combust Flame* 2015;162(5):2231–47.
- [63] Joo H, Gülder Ö. *Combust Flame* 2011;158(3):416–22.
- [64] Gülder ÖL, Intasopa G, Joo HI, Mandatori PM, Bento DS, Vaillancourt ME. *Combust Flame* 2011;158(10):2037–44.
- [65] Flower W, Bowman C, editors. Soot production in axisymmetric laminar diffusion flames at pressures from one to ten atmospheres. *Symposium (International) on Combustion*; 1988: Elsevier.
- [66] Mandatori PM, Gülder ÖL. *Proc Combust Inst* 2011;33(1):577–84.
- [67] Thomson KA, Gülder ÖL, Weekman EJ, Fraser RA, Smallwood GJ, Snelling DR. *Combust Flame* 2005;140(3):222–32.
- [68] He Y, Qi S, Liu S, Xin S, Zhu Y, Wang Z. *Energy Fuels* 2020;35(9):7169–78.